Periodicity in ultrasonic atomization involving beads-fountain oscillations and mist generation: Effects of driving frequency

Xiaolu Wang, Yasushige Mori, Katsumi Tsuchiya *

Dept. of Chemical Engineering and Materials Science, Doshisha Univ., Kyotanabe, Kyoto 610-0321, Japan

ARTICLE INFO

ABSTRACT

Ultrasonic atomization induced by high driving frequency, generally on the order of 1 MHz or higher, could involve a liquid fountain in the form of a corrugated jet, or a chain of "beads" of submillimeter diameter in contact. This study concerns dynamics/instability of such beads fountain, observed under lower input power density (≤ 6 W/cm^2) of the "flat" ultrasound transducer with a "regulating" nozzle equipped, exhibiting time-varying characteristics with certain periodicity. High-speed, high-resolution images are processed for quantitative elucidation: frequency analysis (fast Fourier transform) and time–frequency analysis (discrete wavelet transform) are employed, respectively, to evaluate dominant frequencies of beads-surface oscillations and to reveal factor(s) triggering mist emergence. The resulting time variation in the measured (or apparent) fountain structure, associated with the recurring-beads size scalable to the ultrasound wavelength, subsumes periodic nature predictable from simple physical modeling as well as principle. It is further found that such dynamics in (time-series data for) the fountain structure at given height(s) along a series of beads would *signal* "bursting" of liquid droplets emanating out of a highly deformed bead often followed by a cloud of tiny droplets, or mist. In particular, the bursting appears to be not a completely random phenomenon but should concur with the fountain periodicity with a limited extent of probability.

1. Introduction

Ultrasonic atomization (to be abbreviated in this study as UsA) is often regarded as a means of generating rather uniform distribution of a swarm of small droplets, or mist. In reality, the UsA-generated mist consists of droplets spanning wide ranges of their diameters, from micro- down to nanometers, as has been reported by, *e.g.*, Yano et al. [1], Kobara et al. [2], Sekiguchi et al. [3], Nii and Oka [4], Kudo et al. [5], and Guo et al. [6]. A variety of its applications are evidenced in the fields including: selective separation or concentration of solute from organic solution (*e.g.*, [7]), spray cooling [8], film coating [9,10], preparation of micro- and/or nano-sized powder (*e.g.*, [11]), air purification [12–15], medical applications (*e.g.*, [16–18]), and applications utilizing sonochemical reactions/reactors associated with cavitation (*e.g.*, [19–23]).

Regarding the UsA also as highly energy-efficient in producing small droplets—requiring no external heat input, researchers have paid much attention to the droplet size distribution (DSD) of generated mist, in particular, from an operational viewpoint. For instance, Zhang et al. [24], using an ultrasonic nebulizer with a vibrating tip directed

downwards for spreading tube-guided liquid, examined the effects on the DSD of the UsA input power, the carrier-gas flowrate, the liquid-phase temperature, liquid surface tension and viscosity, among other parameters to suggest possible combination(s) of the optimum operating parameters that control the DSD. Kudo et al. [5] investigated specifically the effects of UsA driving frequency on the DSD to show that the diameter of nano-droplets in mist decreased with increasing ultrasonic frequency. Kooij et al. [25] studied the DSD using three different types of atomizers/nebulizers: surface acoustic wave (SAW) nebulizer, ("Grove"-type) nebulizer chip and (submerged-type) mist maker, and concluded that the DSD was thoroughly determined by the extent and nonlinear structure as well as size distribution of "corrugated ligaments."

An important scientific impact recognized for the UsA stems from one of the above-mentioned applications: Matsuura et al. [26] conducted, for the first time to our knowledge, a study on ethanol separation via the UsA as a concentrating scheme—which should require to preserve specific flavors (thus to be avoided being heated)—of Japanese Sake; subsequently, Sato et al. [7] showed that the concentration of ethanol in the mist after being atomized by high-frequency ultrasound

greatly exceeded that in the original ethanol aqueous solution. Besides concentrating the solution itself, Nii and Oka [4] successfully separated nanoscale solid particles from a mixture of submicron particles in suspensions—thus having attained size-selective particle separation—via UsA and proposed that particles of specific size could be separated by controlling the recovery of atomized droplets under proper UsA conditions. Due to the lack of understanding of the mechanism of UsA, however, it has not been systematically applied in an industrial scale yet.

It has been claimed in the literature (see the specific references below) that selective separation of solute or suspended particles (or surfactants) from a solution can be attained through two possible mechanisms proposed: *capillary-wave* and *cavitation* hypotheses. The former has been supported by, *e.g.*, Qi et al. [27], Collins et al. [28], and Blamey et al. [29]; the latter by, *e.g.*, Neppiras and Noltingk [30], Kojima et al. [21], Ramisetty et al. [31], and Inui et al. [32]. Cavitation bubbles, if present, could contribute to such selective separation from a multicomponent system like alcohol–water solutions—in symbiosis with capillary instabilities—associated with UsA (*e.g.*, [33]); other supportive references of this *conjunction hypothesis* include Boguslavskii and Eknadiosyants [34], Rozenberg [35], Barreras et al. [36], Simon et al. [16,37], Tomita [38], and Zhang et al. [39].

In regard to the DSD of mist generated via UsA, Antonevich [40] proposed that the size of the emitted droplets depended on the mechanism of their release: capillary-wave instability tended to result in smaller and uniform droplets, while cavitation-bubble collapsing could lead to larger droplets of different sizes on the microscale.

Some visual evidence has been reported in regard to the formation of μm-size droplets—pinched off under parametric decay instability of *capillary waves of microscale* [7]—stemming from interfacial oscillations occurring along a perturbed protrusion or a conical fountain/column of solution [36,41]. There has been, however, little direct (visual) evidence that links the mist formation to the occurrence/prevalence of *cavitating bubbles within the liquid fountain* [42,38,37]. Firstly, the presence of cavitation bubbles under sonication—or "active" bubbles of size usually too small to be individually imaged—have been mostly inferred visually from a long-time exposure of the sono[chemical] luminescence, *i.e.*, the extent of sonochemical activity signifying the cavitation yield [19,20,22]. Secondly, a few are available among those cavitation–sonochemistry studies that provide explicit evidence for the simultaneous occurrence of both the cavitation formation and the UsA mist emergence within and out of the liquid fountain, respectively (*e.g.*, [21]).

Over the past decade or so, high-speed imaging techniques have improved significantly, allowing for more detailed UsA processes to be observed. In our earlier visualization experiments [42], the formation of a chain-of-beads fountain was recorded with an ultrahigh-speed video camera [0.25 megaframes/s with the corresponding resolution of 312×260 pixels (4.2 μm/pixel), 0.5-μs exposure; Shimadzu HPV-1]

equipped with a tele-microscope and a xenon lamp focused with an optical lens on the same optical axis as the camera. Fig. 1 shows a series of captured images when a high-frequency transducer with a *flat disk* oscillating at 2.4 MHz was used at a lower input power intensity (2.0 W/cm^2). A cavity—being not clear whether it is comprised of a single void/bubble or a tightly clustered cavitating bubbles—was observed near the central interior of a fountain bead. As this cavity moved across laterally towards the gas–liquid interface, *droplet bursting* eventually occurred. It was hypothesized in this particular case that droplet bursting would originate from cavitation bubbles.

The same line of study has been conducted using a different type of transducer with *focused* ultrasound, often employed in medical applications [38,16,37]. Tomita [38] investigated, through high-speed (as high as 50,000-fps) photography, atomization of a liquid jet generated by interactions of 1-MHz focused ultrasound with a water surface. He identified the threshold conditions for surface elevation and jet breakup associated with drop separation and spray formation. His specific findings include that: a single drop separated from the tip of a jet without spraying; multiple—typically doublet of—beaded water masses were formed, moving upwards to produce a vigorous jet; and cavitation was detected near the center of the primary bead at the jet's leading part, accompanied by fine droplets (*i.e.*, sprayed mist) at the neck between the primary and secondary beads—claimed to occur due to the *collapse of capillary waves*.

Simon et al. [37] conducted high-speed (5,000–30,000-fps) videography using focused transducers as well, with ultrasound waves of *moderate focal* acoustic intensities [mostly between a few and several hundreds of W/cm^2, or at least 180 W/cm^2—a minimum level for atomization to first appear (though inconsistently) at 20°C [16] in liquid encountering an air interface. For the given ranges of ultrasonic frequencies (2.165 mainly, 1.04 and as low as 0.155 MHz) and liquid sound speeds (1.14–1.90 km/s), they reported, in regard to what they call a drop-chain fountain, that atomization is attained when the acoustic intensity exceeds a liquid-dependent threshold; the drop *diameters* approximately *equal* the ultrasonic *wavelengths*; for (seven) different liquids, the atomization threshold was observed to increase with shear viscosity; upon heating water, the time to commence atomization decreases with increasing temperature; and atomized under overpressure, the static pressure has a negative impact on atomization.

Based on those findings, Simon et al. [37] claimed that bubbles, generated by acoustic cavitation (or possibly boiling), should contribute significantly to atomization from the drop-chain fountain, and overviewed on *one version* of UsA mechanism as follows: For a *focused* ultrasound wave, the *radiation force* from the wave induces a protuberance on the liquid surface. As the protuberance prevails, coherent interactions between the waves *incident on and reflected from* the "pressure-release" interface would result in the generation of numerous cavitation bubbles inside the protuberance. Acoustic emissions out of these
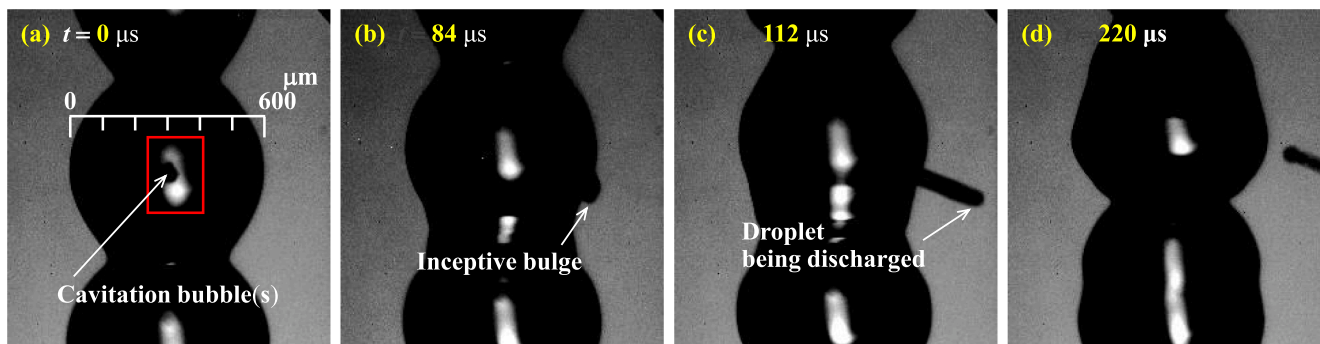

Fig. 1. Selected portion of liquid fountain for 39-wt% (20-mol%) ethanol solution, emanating in the form of a chain of "spherical beads" as the ultrasound (2.4 MHz, 2.0 W/cm^2) is irradiated. Generation of a bursting droplet and deformation of the "host" bead from spherical towards diamond shape: the bursting droplet originates from cavitation bubble(s) moving from central region to lateral surface (gas−liquid interface) of the fountain. The whole process shown at (a) 0, (b) 84, (c) 112 till (d) 220 μs elapsed from an arbitrary time (after [42]).

cavitation bubbles—as they oscillate and collapse—are in turn added separately or synergistically to the surface ripples caused by capillary-wave instabilities, facilitating the droplets pinch-off in atomization.

Deeper insights—spanning physicochemical as well as hydrodynamic aspects—into the involvement of cavitation in driving the UsA could be gained from the two competing mechanisms proposed for the liquid flow associated with the sonic-generated cavitation bubbles underneath a rather flat free surface—thus in the absence of the UsA liquid fountain: 1) acoustic *radiation pressure/*force, as above, in a *traveling*-wave field and 2) acoustic *streaming* in a *standing*-wave field [19,20,22].

Lee et al. [20] in particular, examining three different driving frequencies, 168, 448 and 726 kHz, at a fixed input power of 20 W (1.1 W/cm^2), reported the following trends: at the lower frequency, a strong standing-wave filed prevailed homogeneously along the near central, vertical axis above the transducer, especially at early stages of wave propagation; at the intermediate frequency, the attenuation of acoustic pressure amplitude became appreciable with an increase in the driving frequency, leading to the development of a traveling-wave field near the transducer in competition against the standing wave still prevailing near the free surface; at the higher frequency, the attenuation of the acoustic energy became so significant—developing an energy gradient in the direction of the propagating acoustic wave—that the dominant mechanism shifted, with increasing driving frequency, from the radiation pressure caused by the traveling wave to the acoustic streaming.

Kojima et al. [21] investigated, at a fixed driving frequency of 490 kHz for different input powers of 5–50 W ($\cong$ 0.25–2.5 W/cm^2), the patterns of liquid flow and the spatial distribution of acoustic pressure through a laser Doppler velocimetry (LDV) along with a laser-sheet imaging and through sonochemical luminescence, respectively. With increasing input power (> 1.5 W/cm^2), they demonstrated that a liquid fountain formed with appreciable atomization and that sonochemical luminescence was observable not only in the bulk liquid near the liquid surface but also in the fountain while ultrasonic atomization taking place. It is important to note that all these studies above pointed out crucial roles of cavitation dynamics in association with the above two mechanisms, possibly in explaining some aspects of UsA as well.

While the UsA phenomenon as a whole or, in a series as above, is induced by a constant driving (or excitation) frequency—thus being *inherently periodic* in nature, its characterization in terms of frequency analysis has not been reported extensively (*e.g.*, [27,41]). The very first analysis on the periodicity in the dynamics of liquid drops goes back to the late 19th century; it is Rayleigh's [43] theoretical treatment on small-amplitude oscillations of "free" drops in vacuum (or in the air) that, using spherical harmonic bases, derived—in *linear* approximation—the oscillation frequency of the normal modes; Lamb [44] extended the analysis to a drop oscillating in an immiscible fluid. In recent years, *acoustic levitation* has been extensively employed to investigate drops suspended by an acoustic radiation pressure arising from *nonlinear* effects of intense ultrasound [*e.g.*, [45–47], [48] (for drops levitated by an airflow), [49]].

Trinh et al. [45], in the study of the axisymmetric (small-amplitude shape) oscillations of acoustically levitated liquid drops in an immiscible fluid, measured oscillation frequencies—resonance frequencies of the first few modes—to find them to be in general agreement with theoretical results from linear approximation for low-viscosity liquids (*i.e.*, with negligible viscous damping). Trinh and Wang [46] further found a trend of increasing oscillation frequency of the axisymmetric mode with increasing extent of an *oblate* distortion, suggesting quantitatively a *soft nonlinearity* in the fundamental resonant-mode frequency as the oscillation amplitude is increased.

Shen et al. [47] reported the actively-modulated parametric excitation of *sectorial* oscillations—a category of non-axisymmetric oscillations—of water drops through acoustic levitation at $\cong$ 22 kHz. Their important findings include that: the stable sectorial oscillations were observed to span the oscillation modes from the 2nd up to the 7th mode; the initial oblate drop shape is essential to the given excitations; the

oscillations, not directly driven by external forces, lead to the frequency that increases with the number of mode but decreases with the equatorial radius; their data—the dependence of the measured oscillation frequency, which will coincide with *half* the modulation frequency, on the drop size as well as the oscillation mode—could be well described using the Rayleigh equation [43] modified by replacing the *sphere-equivalent* radius with the initial *equatorial* radius of an oblate drop exhibiting mainly horizontal sectorial oscillations.

The periodicity detectable in the liquid-fountain dynamics can be quantified based on the principle of frequency analysis, where time-series data/signals are decomposed into a series of waves with wavelengths and amplitudes individually specified. If the aim of analysis were just to identify the characteristic/dominant frequencies, the Fourier-transform analysis in terms of power spectrum density would be adequate. The Fourier transform—or its fast, discrete form of algorithm (fast Fourier transform: FFT)—and its inverse establish a one-to-one relationship between the time domain, function $f(t)$, and the frequency domain, spectrum $F(\omega)$. It can be viewed as the decomposition of $f(t)$ into a sum of frequency components, the coefficients of which are given by the inner product of $f(t)$ and $\exp(-i\omega t)$. The spectrum $F(\omega)$ dictates the overall strength/intensity with which each frequency ω is contained in $f(t)$. The Fourier transform, however, does not show how the frequencies vary with time in $f(t)$.

If, on the other hand, the time-series data were to be analyzed to extract essential quantitative features *hidden* in the signals both in *time and frequency* domains and directly linked to the fountain dynamics associated with apparently *ad-hoc* (thus time-dependent) droplet-bursting events, it would be a time–frequency analysis (discrete wavelet transform: DWT) that plays a role (*e.g.*, [50–53]. The wavelet-transform analysis, being able to extract more detailed information, especially time-dependent (such as shift in frequency with time) characteristics of the signals, could provide better physical interpretation of the UsA phenomenon, thus helpful in detecting possible correlations between the rather regularly oscillating fountain surface and the occasionally "triggered" droplets bursting.

Several aspects of the UsA in its fundamental nature have been described thus far: the DSD of emerging mist; the selective separation/concentration of solute (and the alike) into the mist with its extent and mechanism(s); the structure and dynamics of the (general) liquid fountain observed visually; more extensive visual elucidation of the beads-structured fountain associated with internal cavity and/or (external) droplets bursting; and the periodic nature or some dominant frequencies of the fountain-beads (or ideal cases of isolated-drops) oscillations. Among these, it is the present study's intent to focus on quantitatively elucidating the effects of the UsA driving frequency on the structure [including characteristic dimension(s)] and dynamics [*viz.*, characteristic frequency(ies)] of a chain-of-beads fountain realized under lower input power intensity.

To this end, high-speed, high-resolution visualization is utilized to identify the surface dynamics of individual fountain-beads and possible realization of the droplets bursting; both the frequency (FFT) and time–frequency (DWT) analyses are employed to evaluate their periodic characteristics; and some theoretical consideration is made to obtain simple—hopefully predictive—relationships towards providing the ranges of characteristic dimension and frequency as functions of the driving frequency.

2. Experimental

Fig. 2 shows a schematic diagram of the experimental system for ultrasonic atomization. A high-frequency ultrasonic transducer (KAIJO QT-011: 1.0, 2.0 and 3.0 MHz) was set on the bottom of a square vessel; the dimensions of the vessel were 200×200×185 (height) mm. The input power applied to the transducer ranged 4–14 W. A Teflon® nozzle with a conical hollow structure (inner diameter of 2 mm at the top) was installed—to help stabilize the liquid-column formation and
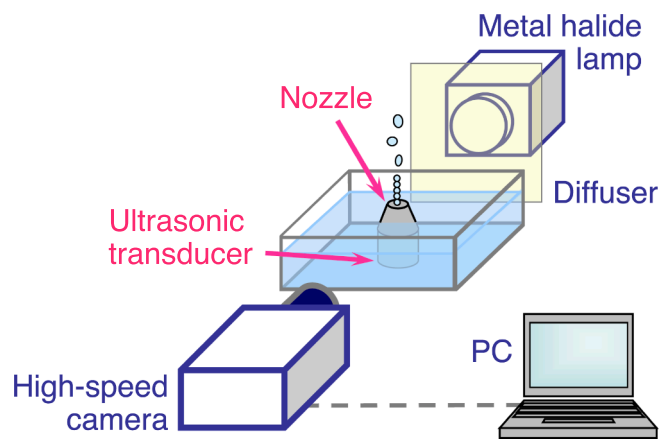
Fig. 2. Schematic diagram of the experimental system for visual observation of liquid fountain.

behavior—directly above the transducer's oscillating disk, a circular element of 20.0 mm in diameter (with an effective oscillating diameter of 16 mm) and 7.5 mm above the bottom. The input power density then ranged 2–7 W/cm^2, which will be exclusively used below as an operating parameter.

The distance from the center of the oscillating disk to the free surface of the solution (effective liquid depth) was 20 mm. The liquid used was an aqueous ethanol solution with initial concentration of 50 wt% (28 mol%), temperature of which was set, before each run, to 25°C in a constant temperature bath. During the UsA over 10 s of operation at most, the bulk ethanol concentration is presumed not to vary, thus the liquid properties kept invariant.

2.1. High-speed visualization

High-speed imaging was made via a digital camera (Photron FAST-CAM MINI AX100) attached with a macro-lens (Nikon Micro-Nikkor 105 mm f/2.8) to observe the dynamics of liquid fountain and the associated phenomena, especially in detecting the ever-changing outline of the fountain surface and the onset position of droplet bursting. Each specific projection was captured—at a frame rate of 20,000 fps (with a resolution of at least 256×512 pixels) and an exposure time of 46.88 μs

(inter-frame time of 3.12 μs)—using a metal halide lamp (Lighterrace MID-25FC) as a light source. The imaging was started 5 s after the transducer was powered and a 0.5-s period of data were recorded. A sheet of light diffuser was installed between the liquid fountain and the lamp, thus reducing the non-uniformity of backlighting.

2.2. Image processing

Fig. 3 shows a sequence of the procedures for image processing and data acquisition. An image analysis software (DITECT Dipp Macro) was used to binarize original images of the liquid column in the air; the threshold for the binarization was set at the brightness level of the "shadow" in the very vicinity of the gas–liquid interface. Filling in blank (s) then extracted the interface boundary/outline, confined by thinning it down to 1 pixel; the centerline of the liquid column was extracted as well. A video analysis software (KEYENCE Movie Editor) was used to determine the shape of an ellipse representing each bead in contact along the liquid column; the lowest two beads above the bottom of the liquid column were regarded stable and equivalent (or representative) spherical diameters of the two were measured in each image; this "vertical" apparent/effective chord length is determined to be the characteristic size of the fountain beads—an average over 60 pieces of the relevant images (30 frames of images with two beads each) obtained under each experimental condition.

2.3. Time-series data analysis

As stated towards the ending of Section 1, the frequency analysis is to in principle decompose a given time-domain signal $f(t)$ into a frequency-domain spectrum $F(\omega)$. In the FFT, the corresponding (to the former) sum of discrete elements, $f_{j+1}(t)$ ($j = 0, 1, \cdots, N-1$), sampled at equal intervals are processed through a fast, efficient algorithm (MathWorks MATLAB®2019b) to obtain the corresponding (to the latter) spectrum:

$$F_{k+1}(\omega) = \sum_{j=0}^{N-1} \Psi^{jk} f_{j+1}(t) \tag{1}$$

where the term specifying the inner product on the right-hand side is given by the jk-th power of $\Psi = e^{-2\pi i/N}$ [54], and the left-hand side thus evaluated provides the power spectrum, $|F(\omega)|^2$, which signifies the spectrum intensity at each frequency.

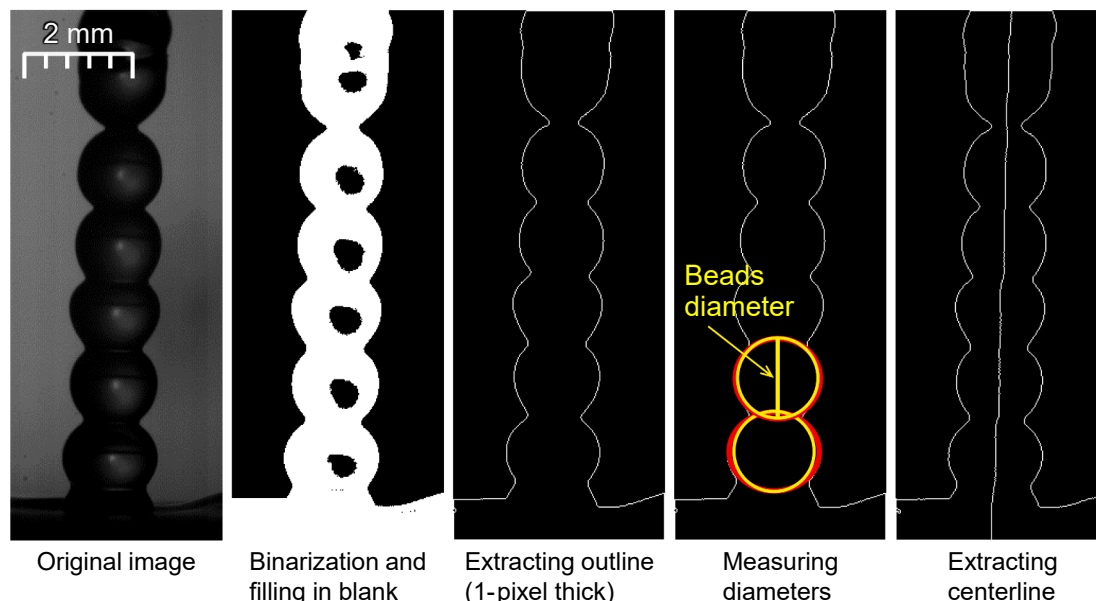Besides the FFT, the DWT employed as a time–frequency analysis is

| Original image | Binarization and filling in blank | Extracting outline (1-pixel thick) | Measuring diameters | Extracting centerline |

Fig. 3. Sequence of image processing involving binarization for determining individual beads diameter.

to be directly applicable to discrete data, expressed as

$$DWf(j,k) = 2^{j/2} \sum_m f_m(t) \psi(2^j t - k) \qquad (2)$$

Here the given time series as a discrete function, $f_m(t)$, is to be transformed by the discrete wavelet operator, $DW(j,k)$, at dyadic scaling (dilation), 2^{-j}, and shifting (translation), $2^{-j}k$, where a pair of parameters/integers (j,k) specify the ranges of "frequency level" and "local time span," respectively. Such method of sequentially decomposing and analyzing the signal $f(t)$ which consists of $N = 2^M$ data in stages of resolution is called multiresolution analysis (MRA).

Wavelets are a family of functions of invariant shape and zero mean that are localized in both the time and frequency domains. The wavelets family is derived from a single prototype function, called the *mother wavelet*, by dilating and translating her (as above). Associated with each wavelet, being a band-pass filter, is a low-pass filter, or *scaling function*. The family of discrete dyadic wavelets, $\psi_{j,k}(t) \equiv 2^{j/2} \psi(2^j t - k)$, thus specified can form a complete orthonormal basis; a usual approach is to select from a library of proven orthonormal basis functions a proper candidate (in this study, Daubechies7 in MATLAB®2019b) so as to best represent the given signal. The wavelet transform—physically interpreted as the signal energy in the region of the time–frequency plane spanned by the selected basis function [55] and called the *discrete wavelet coefficient*, $d_{j,k}$ $[\equiv DWf(j,k)]$—can be inversely transformed to reconstruct the function $f(t)$ as

$$f(t) \approx \sum_j \sum_k d_{j,k} \psi(2^j t - k) \equiv \sum_j g_{1-j}(t) \quad (1 \le j \le M) \qquad (3)$$

That is, the function $f(t)$ is first approximated for the actual numerical scheme by Level/Scale 0 interpolation, $f_0(t)$ $[= g_0(t)]$, which is decomposed into Level -1 *scaling* component, $f_{-1}(t)$, and the Level -1 *wavelet* component, $g_{-1}(t)$. Such a decomposition may be repeated until $j = M$ is reached. In principle, if the signal $f(t)$ consists of 2^M data points, it can be decomposed to Level $-M$ [50,56]. In the present study of MRA, the wavelet decomposition was performed down to Level -9.

3. Results and discussion

The characteristics of liquid fountain and its associated mist observed under the present experimental conditions are described and discussed in both static/time-averaged and dynamic natures, with specific driving frequencies of 1.0, 2.0 and 3.0 MHz (as well as auxiliary ones of 0.43, 0.80, 1.6 and 2.4 MHz) over the range of input power density, 2–7 W/cm²—applied to the UsA transducer.

As demonstrated in Fig. 4 for the case of the highest driving frequency examined, 3.0 MHz, a chain-of-beads fountain [42] is found to be attainable with limited stability in the formation of such a steady beads structure of liquid column—being confined to a range of 3–6 W/cm² (with the specific transducer used): below this range, a series of beads emanating from the so-called "Foundation Region" right above the nozzle [41] are no longer stable; above the range, the beads structure will be disturbed to an extent that it may not be recognized. It is to be noted here that, while the lowest input power density of the said range, 3 W/cm², could lead to the beads fountain, it may not maintain the characteristic aligning stability along the vertical direction of ultrasonic wave propagation from the transducer. In the following, the characterization of the beads fountain as well as the associated mist is prescribed mainly in terms of the three representative driving frequencies in the confined range of applied power density (4, 5 or 6 W/cm² exclusively).

3.1. Phase-averaged size specificity of beads fountain

Fig. 5 shows three series of images of the beads fountain obtained at different driving frequencies when the applied power density is 6 W/cm². With an increase in the driving frequency, the size of beads will decrease drastically. Some specific features of the beads fountain are noted when comparing them between the frequencies: When the frequency is 1.0 MHz, the fountain is mostly characterized by its surface oscillations occurring, for some of the beads, due to the excitation of either local protrusions or capillary waves on the otherwise smooth surface; still, the beads chain basically consists of spheres or ellipsoids.

At 2.0 and 3.0 MHz, in addition to such surface oscillations of the bead, which will be noticeably enhanced—in the form of bead shape itself, two features are clearly detected, *viz.*, the bursting of (rather large) droplets concurring with such shape fluctuations and the noted extent of the Foundation Region. The latter feature is particularly obvious at 3.0 MHz, which implies that the extensive formation of the Foundation Region may promote the droplets bursting. This speculation is supported by Simon et al. [16], who reported that once the "mound" (the same as the Foundation Region) was formed, more significant atomization ensued. From a different perspective, the growth rate of the beads fountain (in relation to ultrasonic surface-wave propagation rate) was measured to be 102, 112 and 183 mm/s; the fountain growth rate at 3.0 MHz was much (by roughly three quarters) faster than those at 1.0 and 2.0 MHz. It is thus believed that there should be some significant
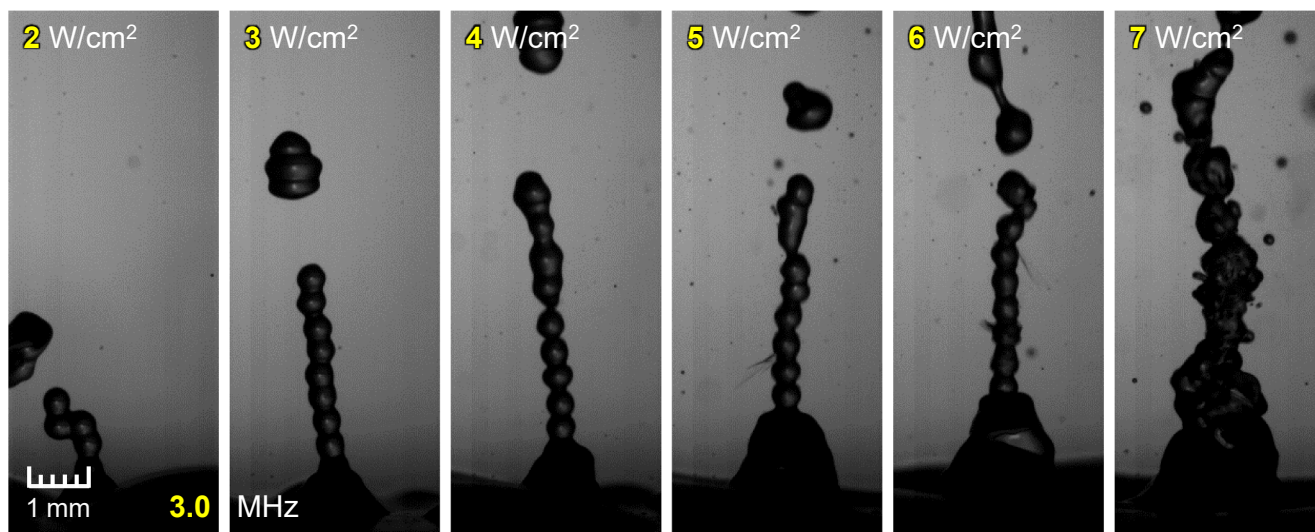

Fig. 4. Images of liquid fountain obtained at different input power densities for driving frequency of 3.0 MHz.
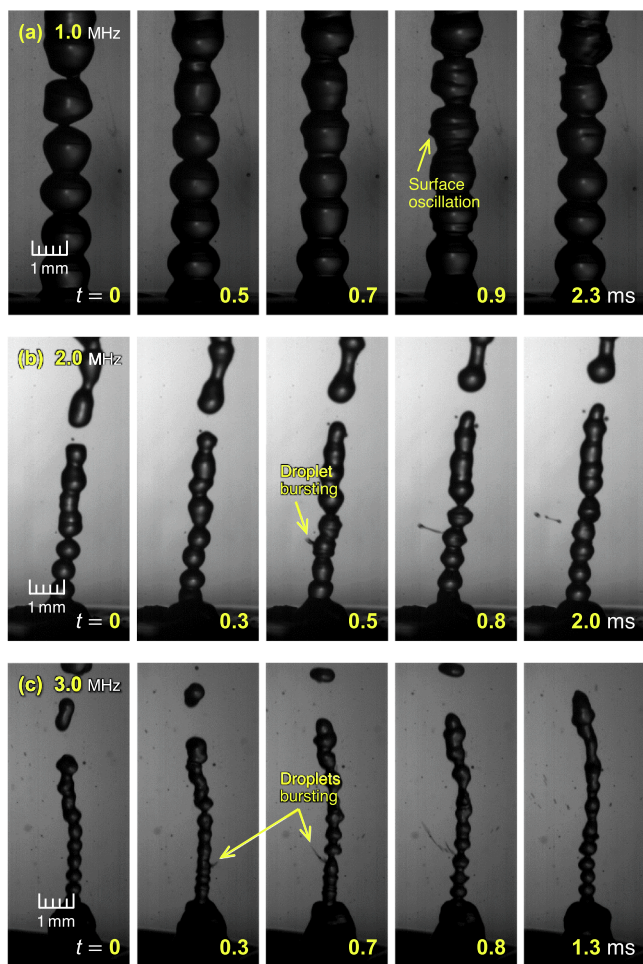
Fig. 5. Time sequences of beads fountain at driving frequencies of (a) 1.0, (b) 2.0 and (c) 3.0 MHz for input power density of 6 W/cm^2.

differences in the bulk and surface dynamics along the liquid fountain caused by those in the UsA driving frequency, which need to be clarified in the future work.

As a general feature, the sizes of chain-beads constituting the liquid fountain are found to be nearly uniform (except for ones associated with the droplet bursting) at each given driving frequency (see Fig. 5), while the fountain tends to repeatedly reproduce longitudinal/transverse shape stretching (vertically cross-sectioned ellipticity) of each bead. Once the contour of each ellipse is determined (see Section 2.2), an apparent diameter of each bead in the *direction of the ultrasonic wave* is estimated as a characteristic length *associated with the wave propagation*. This length (*i.e.*, *vertical* chord length) should then be a proper/effective measure of *wave-inherent*—if indeed it applies so—bead diameter approximated by an imaginary circle completing the outline of "spherical" bead (see Fig. 3), which can also signify on average the liquid-column diameter.

Table 1 lists the measurement results for such "effective" diameter of chain-beads at each of the input power densities of 4, 5 and 6 W/cm^2; the diameters of 60 pieces of beads selected properly (see above) were measured under each condition, for the ultrasonic frequencies of 1.0, 2.0

and 3.0 MHz, to provide three representative average diameters of 1.44, 0.68 and 0.45 mm, respectively. In order to reduce possible human-associated errors in the measurement, three identical sets of measurements were conducted by three persons, which essentially provide consistent results for both the averages and standard deviations. It can be suggested that this characteristic—*wave-inherent*—diameter is rather independent of the applied power density and that—more importantly—it *indeed* will almost coincide with *half* the values of the wavelength of ultrasound being excited by the 1.0-, 2.0- and 3.0-MHz driving frequencies; the pertaining wavelengths are estimated to be 2.94, 1.47 and 0.98 mm, respectively, where the sound speed of 1,470 m/s in 50-wt% ethanol aqueous solution at 25°C [57] is employed.

Thus obtained results are consistent with those reported by Simon et al. [37]. While they used a different type of (focused) ultrasonic transducer with frequencies of 1.04 and mostly 2.165 MHz and applied input power densities about 30 times or greater than the range examined in this study, the resulting fountain was of almost the same range of diameters as the present estimates. In their focused-transducer configuration using water as the liquid phase, a doublet of beads—unlike our chain-of-beads fountain—were formed whose values of diameter were reported to be 1.50 and 0.62 mm, respectively, at the above driving frequencies. It could then be assured that the beads-fountain diameter is to be independent of the type of high-frequency transducer as well as the applied power density but will depend on the driving frequency along with the sound speed of the ultrasonic wave.

In addition to the three frequencies examined (and discussed so far) in the present study, *i.e.*, 1.0, 2.0 and 3.0 MHz, auxiliary tests are made applying lower (< 1 MHz) ultrasonic frequencies of 430 and 800 kHz as well as intermediate ones, 1.6 and 2.4 MHz; note that the former three are generated using the same types of transducer elements from KAIJO described in Section 2, while the last one comes from the transducer (Honda Electronics HM-2412) used in our previous studies [42,58].

Fig. 6 shows the average diameter of the fountain beads obtained under each specific condition tested, plotted as a function of the driving frequency. All the data points, including the auxiliary ones—but excluding the data at the lowest two frequencies, for the average diameters or the characteristic bead diameters (d_{bead}) of 0.85 and 0.60 mm, respectively, at 1.6 and 2.4 MHz as well as the values given in Table 1 tend to follow the physical principle, *viz.*,
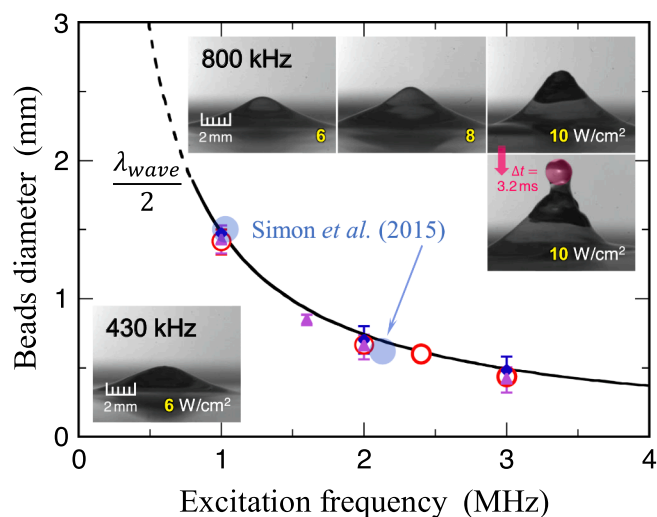
Table 1
Beads diameters for different input powers and ultrasonic frequencies.

Input power (W/cm^2)	4	5	6
1.0 MHz	1452±139 μm	1436±106 μm	1432±109 μm
2.0	675±47	679±76	677±46
3.0	451±49	438±39	453±45

Fig. 6. Decreasing trend in beads diameter with increasing UsA-driving, or ultrasound-excitation, frequency, predicted by that in ultrasound wavelength (experimental data represented by three different symbols to signify three identical sets of measurements, conducted by three persons, which essentially provide consistent results for both the averages and standard deviations, thus with possible human-associated errors minimized in the measurement).

$$2d_{bead} \cong \lambda_{wave} = v_{wave}/f_{wave} \tag{4}$$

where λ_{wave} is the wavelength, v_{wave} the speed, and f_{wave} the frequency of the ultrasound excited by the driving frequency. Here it should be noted that the frequency of the ultrasonic wave f_{wave} realized to prevail—once sufficient instabilities are set in to induce the observed liquid-column fluctuations—will be *half the ultrasonic excitation frequency f_{ex}* [59,27,41,25], which is assumed to be identical to the driving frequency:

$$f_{wave} = f_{ex}/2 \tag{5}$$

It would be of a significant physical implication then to infer that the *contour* of a chain of beads in contact could be represented by a (not space-fixed but) "time-traced" traveling wave axially reflected on both sides, resembling a "virtual" *standing wave* form of nonlinear sinusoidal nature, as can be seen in Fig. 5 in the steady formation region (*i.e.*, the lower part of each image), with its wavelength approximated by the above estimate.

As the driving/excitation frequency f_{ex} is decreased, the characteristic bead diameter d_{bead} increases in line with the hyperbolic variation, depicted by the solid curve in Fig. 6, in the ultrasound wavelength λ_{wave} (for a given liquid, thus fixed v_{wave}). This trend represented by Eq. (4) with Eq. (5) cannot be judged, however, to be realized for the lower f_{ex} of 800 as well as 430 kHz, as no appreciable liquid-fountain formation was observed—above the stabilizing nozzle—under the present experimental conditions (see the inset of Fig. 6 without the nozzle equipped). It is only noted here that the lower 0.43-MHz auxiliary case resulted in merely a gently-sloping swell or mound on otherwise horizontal liquid surface even with increasing input power, while the higher 0.80-MHz case exhibited a sharper protrusion with occasional precursory beads-like protuberance on top of it.

In the latter case, the height of protrusion increased with the input power; at the highest tested in this study (10 W/cm²), the precursory structure—projected as a circle—was evaluated to have an average diameter of 1.88 mm for 30 different occasions (cf. the pink-shaded in the figure inset). Such two cases of unrealized UsA would stem partly from possible failure in attaining the threshold level for the *high directivity*—or more probably, partly from the two mechanisms described in Section 1—acoustic *radiation pressure* and/or acoustic *streaming*—of soundwave induced by applying ultrasound of *high frequency*.

Furthermore, even if the beads fountain could have been formed, the characteristic bead diameter d_{bead} may exceed (or at least comparable to) the capillary length (l_c):

$$l_c = \sqrt{\sigma/\rho_l g} \tag{6}$$

where σ and ρ_l are the surface tension and density of the liquid, respectively, and g the gravitational acceleration. When this condition ($d_{bead} > l_c$) meets (see the dashed part in Fig. 6), the gravitational wave would dominate over the surface-tension/capillary wave. For the present 50-wt% ethanol aqueous solution at 25°C, $l_c = 1.80$ mm with the density and surface tension of 902 kg/m³ and 28.8 mN/m used [60]. The characteristic bead diameter, on the other hand, would be estimated—if exists—to be $d_{bead} \cong \lambda_{wave}/2 = \left(\frac{1}{2}\right)1,470/(800 \times 10^3/2) = 1.84$ mm, thus $d_{bead} > l_c$, for f_{ex} of 800 kHz. It could then be claimed that realizing UsA or the beads fountain requires a minimum driving frequency of at least 0.8 MHz.

3.2. Time-dependent characteristics of beads fountain

When the input power density and/or driving frequency are below given thresholds (but within the present confined ranges), the beads fountain forms, as indicated in the previous section, with almost no atomization detected—but with moderate surface oscillations. As either the input power density or the driving frequency, or both, are raised,

droplets bursting and/or mist spreading would arise from the beads fountain. As shown in Fig. 7(a) at moderate 2.0 MHz, a stable beads fountain is formed—cyclically—at an arbitrarily defined clock time $t = 0$, ~5 s after the onset of ultrasonic irradiation. Subsequently, (b) bursting of a rather large droplet is detected across the surface of a fountain bead, along with the shape and surface state of the bead being altered. These multitude of phenomena are then followed by (c) thrusted spread of clouds of tiny droplets, or mist. While the mist may not be observed (limited by the camera resolution) every time it is generated, it tends to follow the droplets bursting. Such a series of time-sequent result obtained at the highest input power density of the range, 6 W/cm², indicates that the droplet bursting could trigger the mist emergence. This speculation is partly supported by Simon et al. [37], who captured droplet bursting before atomization as well.

The extent of surface oscillations along the beads fountain—or the deformation of each bead itself—signifies the above-stated disturbances observed in the absence and presence of the mist spreading as well as the droplets bursting; such extent is to be quantified for each driving frequency. To extract the extent or the amplitude of bead-surface disturbances or wavy dynamics exclusively, the lateral oscillations (or the left–right swing) of the beads fountain as a whole need to be removed. As depicted in Fig. 8(a), both the contour of the fountain surface and the fountain centerline are extracted based on the image processing described in Section 2.2. The horizontal distance from thus-determined central axis to the surface outline—the *net* amplitude of oscillations—is measured at three different vertical locations (Positions 1, 2 and 3) each fixed; these three positions are selected—above the Foundation Region—to be approximately multiples of the average bead diameter.

Fig. 8(b) shows the time variations, for 1.0, 2.0 and 3.0 MHz at 6 W/cm², of each lateral location thus specified at a given axial position, while Fig. 8(c) and (d) provides the outcome of FFT analysis (see Section 2.3) of beads-fountain oscillations for Positions 1 and 3, respectively. At 1.0 MHz, a "semicircular waveform" is "reproduced" in time series on Position 1, whose outline in time reflects the spatial sequence—in the vertical direction—of the fountain-beads shape. The waveform of nearly the same amplitude is obtained on Position 3 as well; the fountain is relatively stable and of almost no droplets bursting. At 2.0 or 3.0 MHz, a waveform with still stable outline is obtained on Position 1, but non-uniformity of the amplitude becomes appreciable on Positions 2 and 3.

Based on the FFT analysis [Fig. 8(c) and (d)], the beads-fountain oscillations are found to be characterized on Position 1 by essentially a unique dominant frequency for each of the driving frequencies, as provided in Table 2, indicating that the waveform obtained on Position 1 should be the surface wave of the beads fountain itself. As given, the dominant frequency in the surface fluctuations of the beads fountain does increase drastically with an increase in the driving frequency. On Position 3, multitude of peaks are detected at 2.0 and 3.0 MHz. It is to be noted that the droplets bursting will occur mostly out of Position 3 (the uppermost position examined) along the chain, which in turn contributes to disturbing the periodicity of beads-surface motion. Over this frequency band, factors strongly related to the droplets bursting are inevitably concealed.

3.3. Simple model-evaluated periodicity of beads fountain

In Section 3.1, the UsA fountain under the present confined ranges of operation is described to consist of stable, nearly spherical beads, which could be (and have been) regarded as individual liquid drops. Studies on the free oscillations of liquid drops were pioneered by Rayleigh [43], followed by Kelvin [61]. In an idealized situation of a self-resonating spherical liquid drop, which originates from (as a constituent of) a liquid jet being destabilized and performs shape oscillations, Rayleigh [43] derived theoretically—without damping—the resonant angular frequencies ω_n of the drop to be
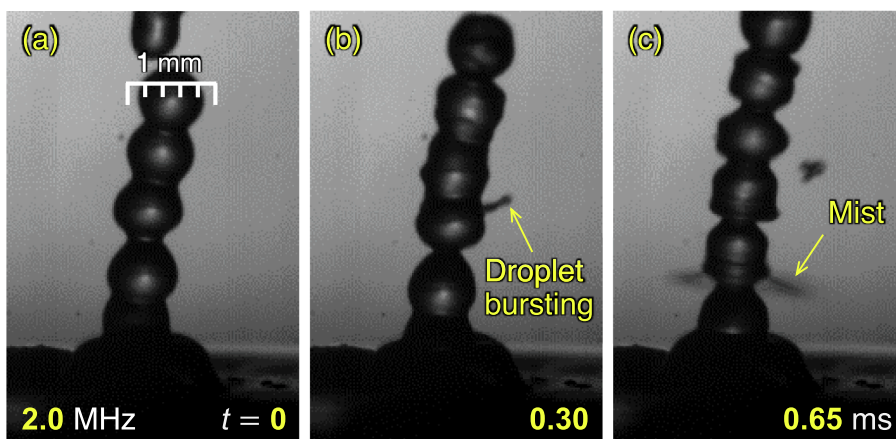
Fig. 7. High-speed imaging of beads fountain with bursting droplet(s) and mist, captured at 2.0 MHz and 6 W/cm²: (a) stable chain-of-beads fountain, (b) droplet bursting from a fountain bead, and (c) succeeding mist spreading and bead deformation.
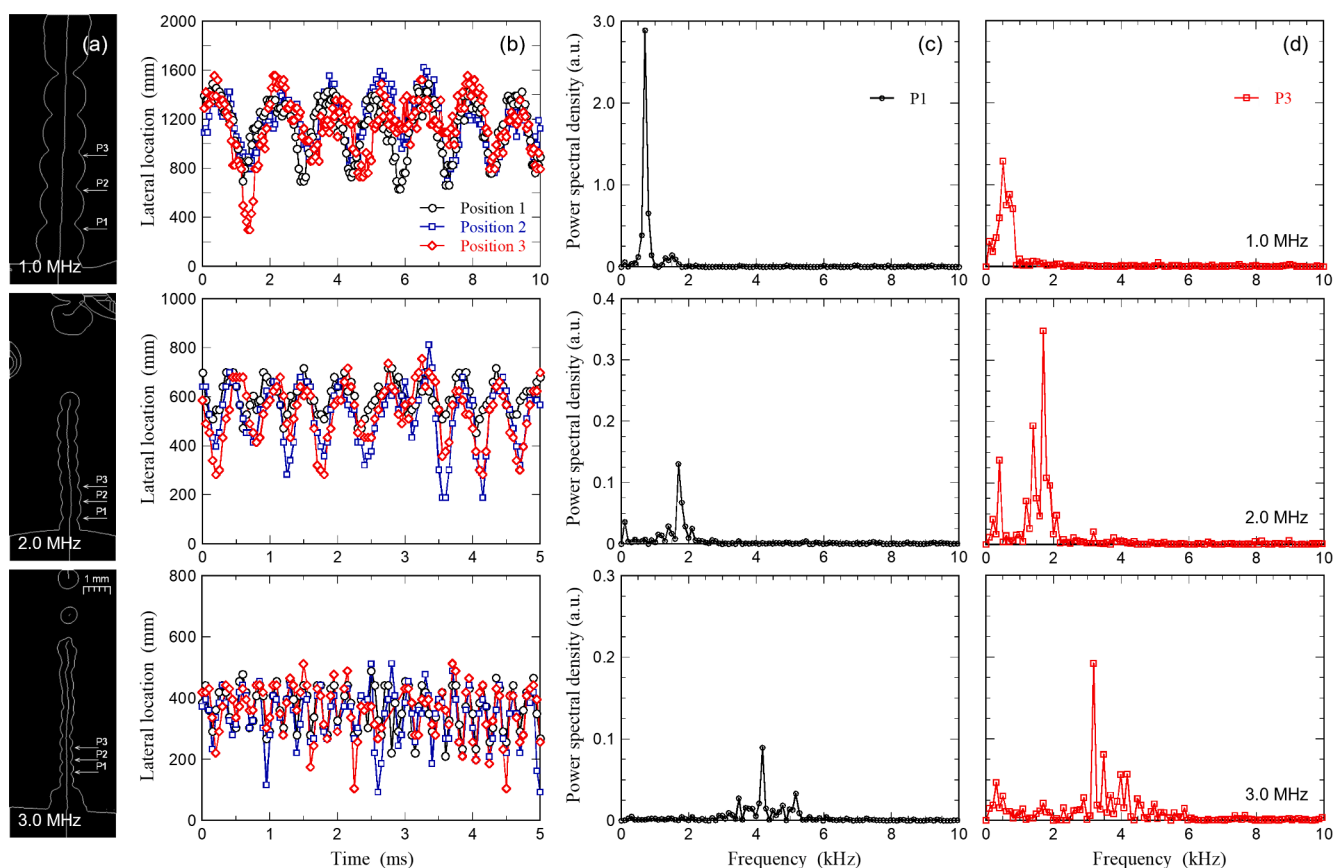

Fig. 8. (a) Net lateral locations—the distances from centerline to surface outline—to be evaluated at three different, fixed vertical locations, or positions denoted as P1, P2 and P3, for driving frequencies of 1.0, 2.0 and 3.0 MHz: values of (P1, P2, P3) = (1.45, 2.9, 4.35), (0.7, 1.4, 2.1) and (0.45, 0.9, 1.35) mm, respectively, above Foundation Region; (b) Time variations in each lateral location thus specified at given axial positions (6 W/cm²); Outcome of FFT analysis of beads-fountain oscillations at (c) Position 1 and (d) Position 3.

$$\omega_n^2 = (2\pi f_n)^2 = n(n-1)(n+2)\frac{\sigma}{\rho_l r_e^3} \qquad (7)$$

where r_e is the equivalent (spherical) radius of the bead/drop. With this size of drop as well as the liquid properties σ and ρ_l specified, the resonance frequencies f_n can be estimated by assigning n, the mode of shape oscillations—the order corresponding to the representative shape of an oscillating drop, whose (vertical in our case) cross section is of, *e.g.*, ellipse: $n = 2$, triangle: $n = 3$, diamond: $n = 4$, pentagon: $n = 5$, and

hexagon: $n = 6$ [47–49].

As inferred from the previous sections, the surface motion of the beads fountain observed in this study is of a resonant nature—*i.e.*, occurring at or (if not completely undamped) near the natural frequency of the beads system—dominated by ultrasound-excited surface waves; the above formula can then be applied to this "beads" system. If applied, the formula would be expressed in terms of an apparent dimensionless number, the resonance Strouhal numbers (Sr_n) based on the resonance frequencies f_n and the drop diameter, which can be replaced by the

Table 2
Comparison of experimental data with predicted values for dominant frequency.

f_{ex} (MHz)	Exp (FFT) Main freq. (kHz)	Exp (DWT) Main freq. (kHz)	Exp (DWT) Bursting freq. (kHz)	Pred [Eq. (7)]		
				f_2 (kHz)	f_4 (kHz)	f_6 (kHz)
1.0	0.70	—	—	0.13	0.38	0.70
2.0	1.70	1.26–2.52	0.32–1.26	0.36	1.08	1.98
3.0	4.20	2.52–5.05	0.63–2.52	0.66	1.99	3.63

individual bead diameter ($2r_e \cong d_{bead}$) in this study, as

$$\pi \, Sr_n = \sqrt{n(n-1)(n+2)} \equiv F(n) \tag{8}$$

with the Strouhal number defined by

$$Sr_n = \frac{f_n d_{bead}}{\sqrt{2\sigma/\rho_l d_{bead}}} = \frac{f_n l_c}{\sqrt{2\sigma/\rho_l l_c}} \left(\frac{d_{bead}}{l_c}\right)^{\frac{3}{2}} \tag{9}$$

It is noted in this equation that the denominator signifies the propagation velocity of a capillary waveform [62] or the so-called capillary–inertial velocity [63], and in this regard the capillary length l_c defined by Eq. (6) is explicitly introduced into the expression, along with the reduced bead diameter. Note also that this dimensionless frequency takes $Sr_n = 0.90$, 2.70 and 4.93 for the mode $n = 2$, 4 and 6, respectively.

Typical patterns of beads deformation observed in the present experiments (at 6 W/cm²) are illustrated in Fig. 9, which signify the time-course shape change of beads fountain prior to atomization being triggered ($t < 0.2$ ms) with *possible* oscillation modes indicated in the figure. Initially, the beads tend to oscillate as if an ellipsoid of prolate-and-oblate oscillation mode ($n = 2$), as shown in Fig. 9(a) and (b); then the beads appear to shift to a diamond-shape mode ($n = 4$), with the radius of curvature on both sides of the beads getting smaller [Fig. 9(c)], followed by the number of bead's "horns" (to be called here) changing from two to four, transitioning to a hexagonal mode ($n = 6$) [Fig. 9(d)]; and eventually, a star shape would give rise to droplets bursting and/or mist spreading [Fig. 9(e)]. The occurrence of oscillation mode $n = 6$ of the beads was confirmed several times before/after the droplets bursting or mist spreading, which is noted to be observed out of a bead (at a time) along the fountain rather than one at its top (cf. [38,37]).

While the mode $n = 6$ of each constituting bead has been frequently detected before or after the droplets bursting, the observed beads are

basically ellipsoidal, accompanying mostly $n = 2$, 4 and 6 modes of oscillations. In comparison to isolated, individual drop oscillations [47], our results show that oscillations tend to be in even modes, due probably to the liquid fountain comprising a chain of beads axially connected.

The results for estimated values of the resonance frequencies f_n, obtained based on the above idealized model and experimentally via the FFT analysis, are compared in Fig. 10. The former—using the Rayleigh [43] equation, Eq. (7), with each of the above three modes of oscillations—leads to three sets of f_n for the UsA driving frequencies of 1.0, 2.0, and 3.0 MHz given in Table 2. In the figure, these series of model prediction are depicted ("cross-plotted") by the three curves, using the direct relationship between f_n and f_{ex} given in the inset. Correspondingly shown is the latter—determined for a rather stable part of the beads fountain on Position 1 (see Section 3.2)—provided in Table 2 as well.

A general agreement between the two series of estimates is encouraging despite the simplicity [of the theory of Rayleigh [43] for linearly perturbed shape oscillations of an isolated spherical drop] vs. the inherent complexity (of the experimental time series as well as FFT signals of nonlinear nature). More specifically, it is tempting to speculate
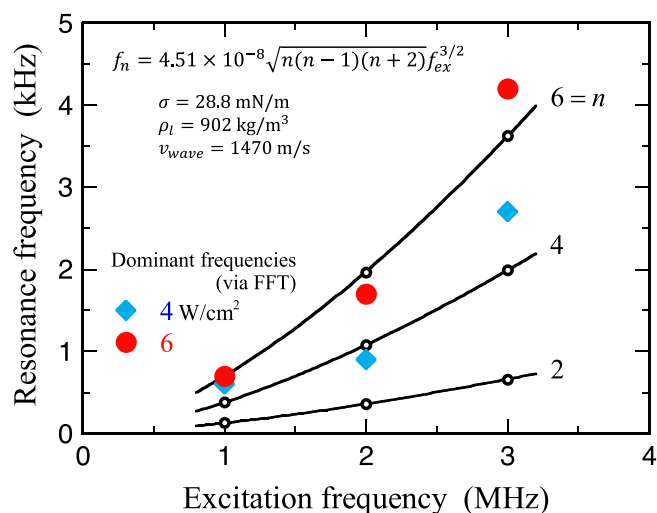
Fig. 10. Possible predictive capability of proposed model equation given in the inset towards representing dominant frequencies evaluated experimentally via FFT.
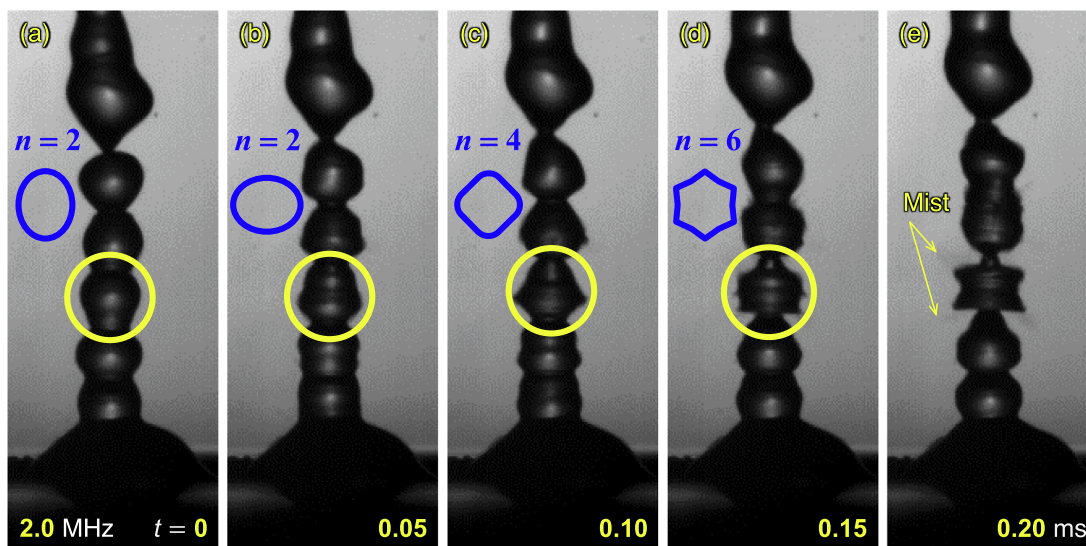
Fig. 9. Typical patterns of beads deformation, signifying time-course shape change of beads fountain before atomization being triggered ($t < 0.2$ ms) with presumed oscillation modes indicated (2.0 MHz, 6 W/cm²).

that the experimentally found dominant frequencies for the three driving frequencies could be reproduced by Eq. (7): for 4 W/cm^2, with $n = 4$—the beads fountain going through a series of diamond-like mode of the beads deformation; for 6 W/cm^2, with $n = 6$—going through a series of hexagonal mode. These sets of numerical coincidence have been visually confirmed in that the droplets bursting and mist spreading—in association with higher-order deformation of the beads fountain—are observed at higher input power density but rarely at the lower.

3.4. Time–frequency characteristics of beads fountain associated with droplets bursting

Above a given vertical position over the Foundation Region, the beads fountain will exhibit not only its surface movement/oscillations but also its associated dynamics such as droplets bursting. As demonstrated in the previous sections, such additional dynamics noticeable (in Fig. 5 or 8 for example) on Position 3 at 2.0-MHz or higher driving frequency(ies) may not be clearly identifiable through separate *time-series* and *frequency-only* analyses. The multitude of frequency bands detected there need to be analyzed more rigorously; to this end, the discrete wavelet transform, DWT—a *time–frequency* analysis—is utilized, which can preserve the time-pertaining information in the frequency analysis (see Section 2.3).

The time-series data [provided in Fig. 8(b) for 2.0 MHz on Position 3 (shown over a 5-ms period), representing the original waveform of the beads-surface motion at 6 W/cm^2 [Fig. 8(a)], is decomposed into wavelets of different frequency bands. Fig. 11 shows the results including (a) the DWT map, spanning 10 levels of frequency band obtained using 2^9 (9-bit) data points for the 9 levels of decomposition (shown in the figure over a 25.6-ms period, corresponding to 256 data points out of the original). Note that the original, zeroth-level, data prior
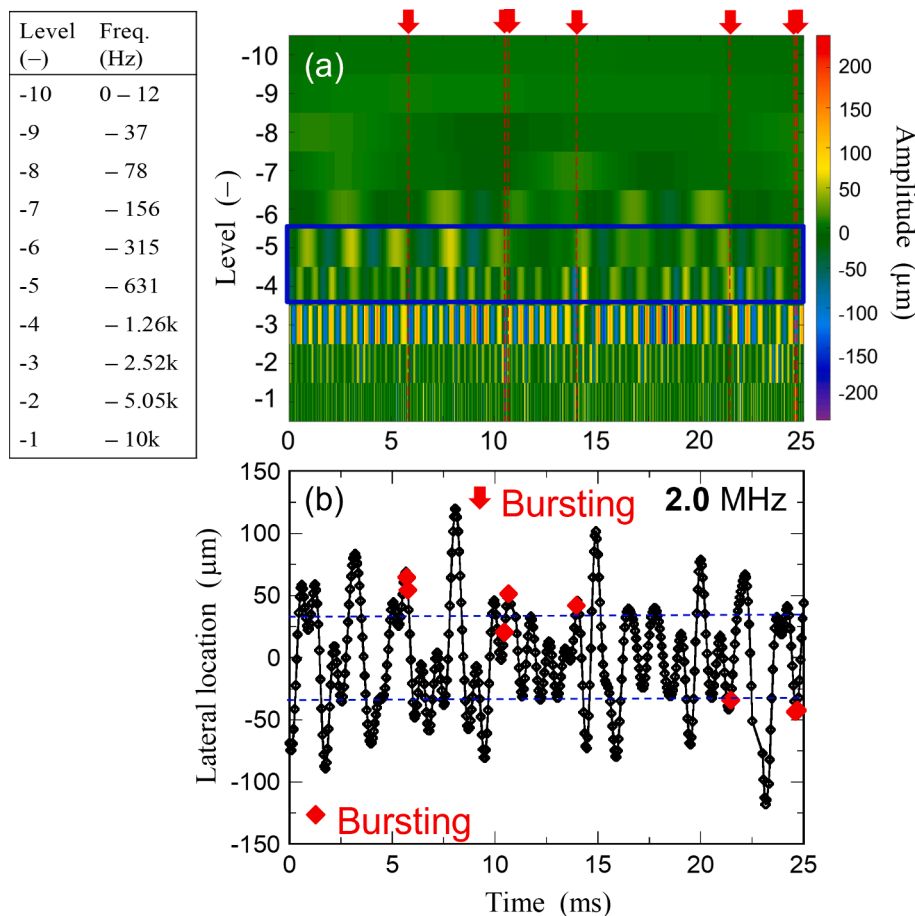
to the first decomposition are not shown, while the last (ninth), lowest-frequency, level represents the 10th scaling component—the remnant of the 9th decomposition—called the approximation coefficient or trend term [56]. The color variation depicted on the map represents the amplitude/intensity variation in each "smoothed" signal (scaling component).

Specifically, Level −3 (for convenience, "−" will be omitted below) spanning the frequency band of 1.26–2.52 kHz signifies—with appreciably high intensity of periodic fluctuations—the dominant frequency detected primarily for the beads surface motion itself. It is to be noted here that the resonance frequency of $f_6 = 1.98$ kHz, estimated from Rayleigh's formula [43], Eq. (7), for the hexagonal deformation mode ($n = 6$, see Table 2), can be said to be a reasonable match.

At higher frequency levels (Level 1 in particular) the fluctuations are presumed to be of noisy nature. At lower frequency levels (Level 4, 5 or as low as 6)—although the average intensity is not as high as that at Level 3, but still noticeable—time-course fluctuations will prevail with reasonable periodicity. To gain a further insight, an attempt has been made to overlap some of the visual information (extracted from the original high-speed images) onto this DWT map; each red arrow along with the dashed line represents the moment at which individual droplet bursting is detected. As could be noticed in Fig. 11(a), the droplets bursting is judged to be associated with some of the fluctuating signals at Level 4 or 5, demonstrating one of the advantages of the DWT analysis, *viz.*, detecting the occurrence of event(s) in time which may not be periodic (quasiperiodic at most).

Fig. 11(b) shows the smoothed signal extracted at Levels 4 and 5 only, spanning the oscillation frequency band 0.32–1.26 kHz. Each event of droplet bursting is marked red. It is found that the bursting tends to occur at or near the peak of rather periodic fluctuations, which should correspond to the resonance frequencies of $f_2 = 0.36$ and/or $f_4 =$

Fig. 11. (a) DWT map for beads-fountain oscillations at Position 3 (2.0 MHz, 6 W/cm^2) with color variation depicted on the map representing amplitude variation in each "smoothed" signal. Each level represents different frequency band as indicated on the left. Each red arrow and dashed line represent the moment for each droplet bursting. (b) Reconstructed time-series data spanning Levels −4 and −5 for waveform given by fountain surface oscillations at Position 3. Blue dashed lines mark average amplitude of ±34 μm.

1.08 kHz, predicted in the same manner as above, for the two lower modes (see Table 2). The droplets bursting, however, appears to be a rather rare event. As a minimum requirement/criterion for the instability to set in towards the bursting, an average amplitude of the *net* lateral fluctuations (see Section 3.2) spanning ±34 μm in this case (the dashed blue lines in the figure) may play a role. Beyond this range, the number of peaks detected is greatly reduced from the total number, as shown in Fig. 11(b), due to the prevalence of a large fraction of smaller-amplitude fluctuations. The number of droplets bursting detected would then account for roughly 30% of the "larger" peaks at most in the beads-fountain oscillations.

The corresponding wavelet decomposition for higher driving-frequency (3.0-MHz) case is given in Fig. 12. The following comparisons against the case given in Fig. 11 can be made: 1) the dominant frequency ranges in 2.52–5.05 kHz (Level 2)—signified with a reasonable agreement to Rayleigh's prediction [43] of $f_6 = 3.63$ kHz [Fig. 12 (a)]; 2) the wavelets extracted from Levels 3 and 4, spanning the frequency band 0.63–2.52 kHz, would be associated with the droplets bursting [marked red in Fig. 12(a) and (b)], occurring—not necessarily—at or near the peaks signified with the resonance frequencies of $f_2 = 0.66$ and/or $f_4 = 1.99$ kHz predicted; and 3) the droplets bursting, being still a rare event (though with larger absolute number than the lower driving-frequency case), with the bursting number accounting for roughly 20% of the "larger" peaks in the beads-fountain oscillations.

While the present findings in regard to the droplets bursting (and the associated mist spreading) are qualitative at this stage, it can be stated at least that the bursting appears to be not a completely random phenomenon but should concur with the fountain periodicity with a limited extent of probability. Furthermore, the beads-fountain oscillations

should be a necessary step for triggering the droplets bursting (one-way coupling) at lower driving frequency, on one hand. The bursting in turn may influence the amplitude and frequency of the fountain oscillations (two-way coupling) at higher driving frequency, on the other hand, leading to the complex dynamics observe in this study. One such complex aspect lies in an experimental finding (not indicated in the discussion so far) that the moment and the local location of triggering the droplets bursting (and possibly the succeeding mist spreading) may not necessarily concur with those of "extremes" of the beads-surface oscillations, represented in Figs. 11 and 12 as "peaks" in the time-series data. Further clarification is definitely needed.

4. Concluding remarks

Upon ultrasonic irradiation under confined operating conditions—driving frequencies of 1–3 MHz and input power densities of 3–6 W/cm^2, the UsA fountain takes the form of *a chain of* "*beads*" in contact, recurring steadily; associated with this cyclic aspect of UsA, droplets bursting and/or mist spreading would arise from the beads fountain, with limited periodicity and probability, as the driving frequency and/or the input power are increased.

The recurring beads themselves are characterized by the UsA *wave-inherent*, "effective" dimension. This *effective beads diameter* is found to almost coincide with *half* the UsA wavelength, which can be specified by *half* the UsA excitation/driving frequency. This predictive scheme is realized via physical principle that the wavelength decreases in inverse proportion to the increasing frequency for a given liquid (thus for a fixed ultrasound speed). The scheme appears to hold as long as the beads diameter will not exceed the capillary length—*i.e.*, provided the
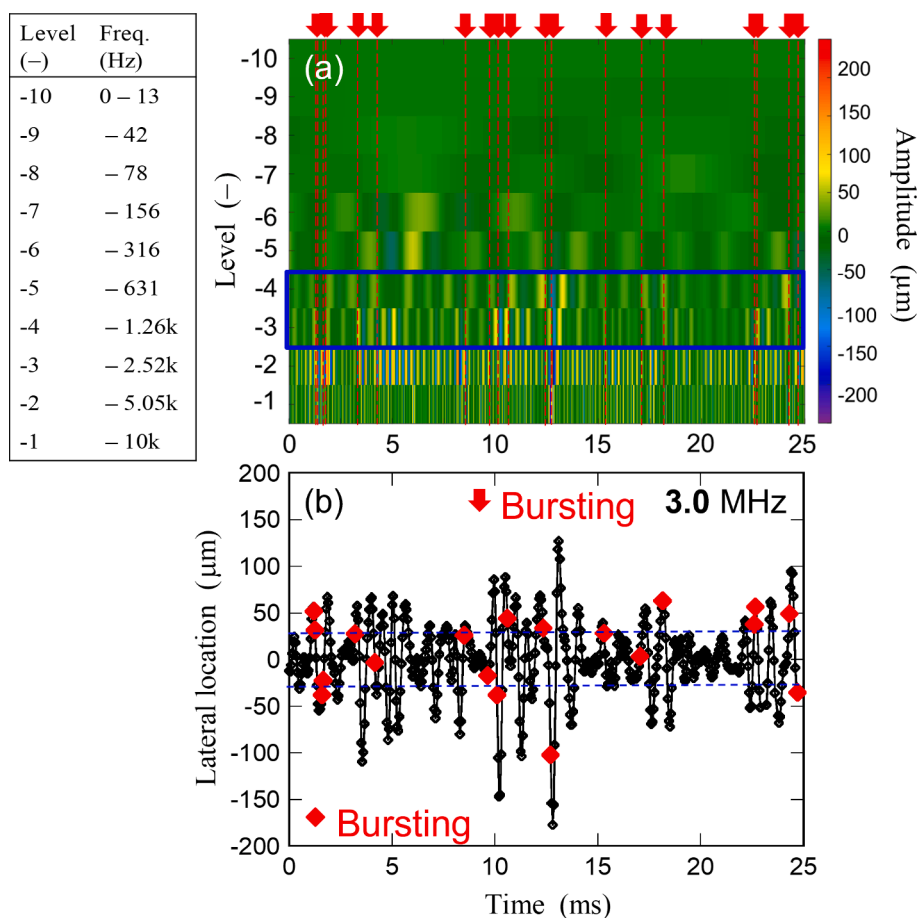

Fig. 12. (a) DWT map for beads-fountain oscillations at Position 3 (3.0 MHz, 6 W/cm^2). See Fig. 11 for details. (b) Reconstructed time-series data spanning Levels −3 and −4 for waveform given by fountain surface oscillations at Position 3. Blue dashed lines mark average amplitude of ±29 μm.

fountain-surface wave is of capillary nature—which could be assured for the driving frequency greater than at least 0.8 MHz.

The cyclic properties of the UsA beads fountain, visually exhibited via high-speed imaging, are characterized by the dominant frequency obtained (FFT-evaluated) experimentally. This *primary* periodicity is found to be well predicted based on the simple theoretical model proposed by Rayleigh [43] with a proper assignment of the mode of cyclic deformation of the fountain beads themselves.

The *secondary* dynamic characteristics associated with the primary beads-fountain periodicity—droplets bursting and/or mist spreading—involve some limited probability and triggering. While the present time–frequency analysis, via DWT, failed to reach their quantitative elucidation due to their complexity, some requirement(s) are identified in terms of higher probability for the droplets bursting to be triggered.

CRediT authorship contribution statement

Xiaolu Wang: Data curation, Investigation, Validation, Writing – original draft. **Yasushige Mori:** Supervision. **Katsumi Tsuchiya:** Conceptualization, Methodology, Validation, Writing – review & editing, Supervision, Project administration.

Declaration of Competing Interest

The authors declare that they have no known competing financial interests or personal relationships that could have appeared to influence the work reported in this paper.

References

[1] Y.F. Yano, J. Douguchi, A. Kumagai, T. Iijima, Y. Tomida, T. Miyamoto, K. Matsuura, In situ X-ray diffraction measurements of the capillary fountain jet produced via ultrasonic atomization, J. Chem. Phys. 125 (17) (2006) 174705, https://doi.org/10.1063/1.2363188.

[2] H. Kobara, M. Tamiya, A. Wakisaka, T. Fukazu, K. Matsuura, Relationship between the size of mist droplets and ethanol condensation efficiency at ultrasonic atomization on ethanol−water mixtures, AIChE J. 56 (2010) 810–814, https://doi.org/10.1002/aic.12008.

[3] K. Sekiguchi, D. Noshiroya, M. Handa, K. Yamamoto, K. Sakamoto, N. Namiki, Degradation of organic gases using ultrasonic mist generated from TiO₂ suspension, Chemosphere 81 (1) (2010) 33–38, https://doi.org/10.1016/j.chemosphere.2010.07.009.

[4] S. Nii, N. Oka, Size-selective separation of submicron particles in suspensions with ultrasonic atomization, Ultrason. Sonochem. 21 (6) (2014) 2032–2036, https://doi.org/10.1016/j.ultsonch.2014.03.033.

[5] T. Kudo, K. Sekiguchi, K. Sankoda, N. Namiki, S. Nii, Effect of ultrasonic frequency on size distributions of nanosized mist generated by ultrasonic atomization, Ultrason. Sonochem. 37 (2017) 16–22, https://doi.org/10.1016/j.ultsonch.2016.12.019.

[6] Y. Guo, X. Yang, G. Li, J. Yang, L.u. Liu, L. Chen, B. Li, Shear turbulence controllable synthesis of aggregated nano-particles using a swirling vortex flow reactor assisted by ultrasound irradiation, Chem. Eng. J. 405 (2021) 126914, https://doi.org/10.1016/j.cej.2020.126914.

[7] M. Sato, K. Matsuura, T. Fujii, Ethanol separation from ethanol−water solution by ultrasonic atomization and its proposed mechanism based on parametric decay instability of capillary wave, J. Chem. Phys. 114 (5) (2001) 2382–2386, https://doi.org/10.1063/1.1336842.

[8] B.S. Arun, V. Mariappan, V. Maisotsenko, Experimental study on combined low temperature regeneration of liquid desiccant and evaporative cooling by ultrasonic atomization, Int. J. Refrig. 112 (2020) 100–109, https://doi.org/10.1016/j.ijrefrig.2019.11.023.

[9] R. Guan, F. Zou, Z. Weng, P. Zhou, Y. Liao, Z. Su, L. Huang, On a highly reproducible, broadband nanocomposite ultrasonic film sensor fabricated by ultrasonic atomization-assisted spray coating, Adv. Eng. Mater. 22 (11) (2020) 2000462, https://doi.org/10.1002/adem.v22.1110.1002/adem.202000462.

[10] S. Khan, S. Chen, Y. Ma, M. ul Haq, Y. Li, M. Nisar, R. Khan, Y. Liu, J. Wang, G. Han, Structural and hydrophilic properties of TiN films prepared by ultrasonic atomization assisted spray method under low temperature, Surf. Coat. Technol. 393 (2020) 125824, https://doi.org/10.1016/j.surfcoat.2020.125824.

[11] Z. Cai, X. Wang, Z. Zhang, Y. Han, J. Luo, M. Huang, B.W. Zhang, Y. Hou, Large-scale and fast synthesis of nano-hydroxyapatite powder by a microwave-hydrothermal method, RSC Adv. 9 (24) (2019) 13623–13630, https://doi.org/10.1039/c9ra00091g.

[12] W.H. Tay, K.K. Lau, A.M. Shariff, High frequency ultrasonic-assisted CO₂ absorption in a high pressure water batch system, Ultrason. Sonochem. 33 (2016) 190–196, https://doi.org/10.1016/j.ultsonch.2016.04.004.

[13] W.H. Tay, K.K. Lau, A.M. Shariff, High performance promoter-free CO₂ absorption using potassium carbonate solution in an ultrasonic irradiation system, J. CO₂ Util. 21 (2017) 383–394, https://doi.org/10.1016/j.jcou.2017.08.003.

[14] J. Wei, J. Gu, J. Guo, W. Li, C. Wang, J. Zhang, Simultaneous removal of nitrogen oxides and sulfur dioxide using ultrasonically atomized hydrogen peroxide, Environ. Sci. Pollut. Res. 26 (22) (2019) 22351–22361, https://doi.org/10.1007/s11356-019-05531-1.

[15] M.M. Marjanian, S. Shahhosseini, A. Ansari, Investigation of the ultrasound assisted CO₂ absorption using different absorbents, Process Saf. Environ. Prot. 149 (2021) 277–288, https://doi.org/10.1016/j.psep.2020.10.054.

[16] J.C. Simon, O.A. Sapozhnikov, V.A. Khokhlova, Y.-N. Wang, L.A. Crum, M. R. Bailey, Ultrasonic atomization of tissue and its role in tissue fractionation by high intensity focused ultrasound, Phys. Med. Biol. 57 (23) (2012) 8061–8078, https://doi.org/10.1088/0031-9155/57/23/8061.

[17] A. Dalmoro, A.A. Barba, M. d'Amore, Analysis of size correlations for microdroplets produced by ultrasonic atomization, Sci. World J. 2013 (2013) 1–7, https://doi.org/10.1155/2013/482910.

[18] E. Perra, E. Lampsijärvi, G. Barreto, M. Arif, T. Puranen, E. Hæggström, K.P. H. Pritzker, H.J. Nieminen, Ultrasonic actuation of a fine-needle improves biopsy yield, Sci. Rep. 11 (2021) 8234, https://doi.org/10.1038/s41598-021-87303-x.

[19] J. Lee, K. Yasui, T. Tuziuti, T. Kozuka, A. Towata, Y. Iida, Spatial distribution enhancement of sonoluminescence activity by altering sonication and solution conditions, J. Phys. Chem. B 112 (48) (2008) 15333–15341, https://doi.org/10.1021/jp8060224.

[20] J. Lee, M. Ashokkumar, K. Yasui, T. Tuziuti, T. Kozuka, A. Towata, Y. Iida, Development and optimization of acoustic bubble structures at high frequencies, Ultrason. Sonochem. 18 (1) (2011) 92–98, https://doi.org/10.1016/j.ultsonch.2010.03.004.

[21] Y. Kojima, Y. Asakura, G. Sugiyama, S. Koda, The effects of acoustic flow and mechanical flow on the sonochemical efficiency in a rectangular sonochemical reactor, Ultrason. Sonochem. 17 (6) (2010) 978–984, https://doi.org/10.1016/j.ultsonch.2009.11.020.

[22] Y. Son, M. Lim, M. Ashokkumar, J. Khim, Geometric optimization of sonoreactors for the enhancement of sonochemical activity, J. Phys. Chem. C 115 (10) (2011) 4096–4103, https://doi.org/10.1021/jp110319y.

[23] J. Choi, J. Khim, B. Neppolian, Y. Son, Enhancement of sonochemical oxidation reactions using air sparging in a 36 kHz sonoreactor, Ultrason. Sonochem. 51 (2019) 412–418, https://doi.org/10.1016/j.ultsonch.2018.07.032.

[24] Y.u. Zhang, S. Yuan, L. Wang, Investigation of capillary wave, cavitation and droplet diameter distribution during ultrasonic atomization, Exp. Therm. Fluid Sci. 120 (2021) 110219, https://doi.org/10.1016/j.expthermflusci.2020.110219.

[25] S. Kooij, A. Astefanei, G.L. Corthals, D. Bonn, Size distributions of droplets produced by ultrasonic nebulizers, Sci. Rep. 9 (2019) 6128, https://doi.org/10.1038/s41598-019-42599-8.

[26] K. Matsuura, M. Kobayashi, M. Hirotsune, M. Sato, H. Sasaki, K. Shimizu, New separation technique under normal temperature and pressure using an ultrasonic atomization, Jpn Soc. Chem. Eng. Symp. Ser. 46 (1995) 44–49.

[27] A. Qi, L.Y. Yeo, J.R. Friend, Interfacial destabilization and atomization driven by surface acoustic waves, Phys. Fluids 20 (7) (2008) 074103, https://doi.org/10.1063/1.2953537.

[28] D.J. Collins, O. Manor, A. Winkler, H. Schmidt, J.R. Friend, L.Y. Yeo, Atomization off thin water films generated by high-frequency substrate wave vibrations, Phys. Rev. E 86 (2012) 056312, https://doi.org/10.1103/PhysRevE.86.056312.

[29] J. Blamey, L.Y. Yeo, J.R. Friend, Microscale capillary wave turbulence excited by high frequency vibration, Langmuir 29 (11) (2013) 3835–3845, https://doi.org/10.1021/la304608a.

[30] E.A. Neppiras, B.E. Noltingk, Cavitation produced by ultrasonics: theoretical conditions for the onset of cavitation, Proc. Phys. Soc. B 64 (12) (1951) 1032–1038, https://doi.org/10.1088/0370-1301/64/12/302.

[31] K.A. Ramisetty, A.B. Pandit, P.R. Gogate, Investigations into ultrasound induced atomization, Ultrason. Sonochem. 20 (1) (2013) 254–264, https://doi.org/10.1016/j.ultsonch.2012.05.001.

[32] A. Inui, A. Honda, S. Yamanaka, T. Ikeno, K. Yamamoto, Effect of ultrasonic frequency and surfactant addition on microcapsule destruction, Ultrason. Sonochem. 70 (2021) 105308, https://doi.org/10.1016/j.ultsonch.2020.105308.

[33] D.M. Kirpalani, F. Toll, Revealing the physicochemical mechanism for ultrasonic separation of alcohol−water mixtures, J. Chem. Phys. 117 (8) (2002) 3874–3877, https://doi.org/10.1063/1.1495849.

[34] Yu Ya Boguslavskii, O.K. Eknadiosyants, Physical mechanism of the acoustic atomization of a liquid, Sov. Phys. Acoust. 15 (1969) 14–21.

[35] L.D. Rozenberg (Ed.), Physical principles of ultrasonic technology, 2, 4−88 Springer (1973).

[36] F. Barreras, H. Amaveda, A. Lozano, Transient high-frequency ultrasonic water atomization, Exp. Fluids 33 (3) (2002) 405–413, https://doi.org/10.1007/s00348-002-0456-1.

[37] J.C. Simon, O.A. Sapozhnikov, V.A. Khokhlova, L.A. Crum, M.R. Bailey, Ultrasonic atomization of liquids in drop-chain acoustic fountains, J. Fluid Mech. 766 (2015) 129–146, https://doi.org/10.1017/jfm.2015.11.

[38] Y. Tomita, Jet atomization and cavitation induced by interactions between focused ultrasound and a water surface, Phys. Fluids 26 (9) (2014) 097105, https://doi.org/10.1063/1.4895902.

[39] H. Zhang, X. Zhang, X. Yi, F. He, F. Niu, P. Hao, Dynamic behaviors of droplets impacting on ultrasonically vibrating surfaces, Exp. Therm. Fluid Sci. 112 (2020) 110019, https://doi.org/10.1016/j.expthermflusci.2019.110019.

[40] J.N. Antonevich, Ultrasonic atomization of liquids, IRE Trans. Ultrasonic Eng. PGUE-7 6–15 (1959).

[41] K. Tsuchiya, H. Hayashi, K. Fujiwara, K. Matsuura, Visual analysis of ultrasonic atomization and its associated phenomena, Earozoru Kenkyu, J. Aerosol. Res. Japan. 26 (2011) 11–17, https://doi.org/10.11203/jar.26.11.

[42] K. Fujita, K. Tsuchiya, Cavitating bubble inside liquid fountain of beads associated with ultrasonic atomization, in: Proc. 8th Int. Conf. Multiphase Flow (ICMF 2013), Paper 863/1–5 (2013).

[43] L. Rayleigh (J. W. Strutt), On the capillary phenomena of jets, Proc. R. Soc. Lond., 29 (1879) 71−97. https://doi.org/10.1098/rspl.1879.0015.

[44] H. Lamb. Hydrodynamics, 6th ed., Cambridge University Press, Cambridge, England, 1932.

[45] E. Trinh, A. Zwern, T.G. Wang, An experimental study of small-amplitude drop oscillations in immiscible liquid systems, J. Fluid Mech. 115 (1982) 453–474, https://doi.org/10.1017/S0022112082000858.

[46] E. Trinh, T.G. Wang, Large-amplitude free and driven drop-shape oscillations: experimental observations, J. Fluid Mech. 122 (1982) 315–338, https://doi.org/10.1017/S0022112082002237.

[47] C.L. Shen, W.J. Xie, B. Wei, Parametrically excited sectorial oscillation of liquid drops floating in ultrasound, Phys. Rev. E 81 (2010) 046305, https://doi.org/10.1103/PhysRevE.81.046305.

[48] W. Bouwhuis, K.G. Winkels, I.R. Peters, P. Brunet, D. van der Meer, J.H. Snoeijer, Oscillating and star-shaped drops levitated by an airflow, Phys. Rev. E 88 (2013) 023017, https://doi.org/10.1103/PhysRevE.88.023017.

[49] A. Watanabe, K. Hasegawa, Y. Abe, Contactless fluid manipulation in air: droplet coalescence and active mixing by acoustic levitation, Sci. Rep. 8 (2018) 10221, https://doi.org/10.1038/s41598-018-28451-5.

[50] C.K. Chui, An Introduction to Wavelets, Academic Press, New York, NY, 1992 https://www.elsevier.com/books/an-introduction-to-wavelets/chui/978-0-12-174584-4.

[51] I. Daubechies, Ten Lectures on Wavelets, Society for Industrial and Applied Mathematics (SIAM) Press, Philadelphia, PA (1992). https://doi.org/10.1137/1.9781611970104. https://epubs.siam.org/doi/book/10.1137/1.9781611970104.

[52] K. Tsuchiya, S. Ide, Y. Mori, T. Saito, Time–frequency analysis of local fluctuations induced by bubble flow, Proc. 10th APCChE Cong., Paper (2004) 4E–05. https://www.jstage.jst.go.jp/article/apcche/2004/0/2004_0_198/_pdf.

[53] H. Liu, K. Wang, A study of characteristic extraction for transformer oscillation wave based on DWT analysis, J. Phys. Conf. Ser. 1311 (1) (2019) 012014, https://doi.org/10.1088/1742-6596/1311/1/012014.

[54] D.B. Percival, A.T. Walden. Wavelet Methods for Time Series Analysis, Cambridge University Press, Cambridge, UK, 2000, https://doi.org/10.1017/CBO9780511841040 https://www.cambridge.org/core/books/wavelet-methods-for-time-series-analysis/A2018601E6907DE4953EEF7A5D0359E5.

[55] B.R. Bakshi, H. Zhong, P. Jiang, L.-S. Fan, Analysis of flow in gas–liquid bubble columns using multi-resolution methods, Chem. Eng. Res. Des. 73 (1995) 608–614.

[56] MathWorks®, "MATLAB® Wavelet Toolbox™, Discrete Multiresolution Analysis, Practical Introduction to Multiresolution Analysis," Help Center R2021a, Natick, MA (2021). https://jp.mathworks.com/help/wavelet/index.html?lang=en.

[57] M. Mijaković, B. Kežić, L. Zoranić, F. Sokolić, A. Asenbaum, C. Pruner, E. Wilhelm, A. Perera, Ethanol−water mixtures; ultrasonics, Brillouin scattering and molecular dynamics, J. Mol. Liq. 164 (1–2) (2011) 66–73, https://doi.org/10.1016/j.molliq.2011.06.009.

[58] K. Satomi, Y. Mori, K. Tsuchiya, Ultrasonic atomization—its structure and dynamics associated with liquid fountain of corrugated beads, in: Proc. 10th Int. Conf. Multiphase Flow (ICMF 2019), Paper 178489 (2019).

[59] R.J. Lang, Ultrasonic atomization of liquids, J. Acoust. Soc. Am. 34 (1) (1962) 6–8, https://doi.org/10.1121/1.1909020.

[60] I.S. Khattab, F. Bandarkar, M.A.A. Fakhree, A. Jouyban, Density, viscosity, and surface tension of water−ethanol mixtures from 293 to 323K, Korean J. Chem. Eng. 29 (6) (2012) 812–817, https://doi.org/10.1007/s11814-011-0239-6.

[61] L. Kelvin (W. Thomson), Oscillations of a liquid sphere, Math. Phys. Papers, 3 (1890) 384−386.

[62] L.-S. Fan, K. Tsuchiya, Bubble Wake Dynamics in Liquids and Liquid–Solid Suspensions, Butterworth–Heinemann, Stoneham, MA (1990). https://www.sciencedirect.com/book/9780409902860/bubble-wake-dynamics-in-liquids-and-liquid-solid-suspensions.

[63] F. Liu, G. Ghigliotti, J.J. Feng, C.-H. Chen, Numerical simulations of self-propelled jumping upon drop coalescence on non-wetting surfaces, J. Fluid Mech. 752 (2014) 39–65, https://doi.org/10.1017/jfm.2014.320.